Bachelor Project

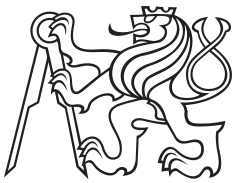

Czech
Technical
University
in Prague

F3

Faculty of Electrical Engineering
Department of Control Engineering

Manipulation with objects on a surface of a liquid using an array of ultrasonic transducers

Josef Matouš

Supervisor: Ing. Tomáš Michálek
Field of study: Cybernetics and Robotics
Subfield: Systems and Control
May 2018

Acknowledgements

First of all, I would like to thank my supervisor, Ing. Tomáš Michálek, for leading this project and consulting everything from designing the experimental platform to academic writing. Additional thanks to other members of the AA4CC research group, namely Ing. Martin Gurtner, Ing. Filip Richter and Ing. Jiří Zemánek, for advice on 3D-printing and laser-engraving.

I must not forget to thank my family and friends for their support and occasional proofreading.

Declaration

I declare that I wrote the presented thesis on my own and that I cited all the used information sources in compliance with the Methodical instructions about the ethical principles for writing an academic thesis.

Prague, 23. May 2018

Abstract

This thesis investigates the use of the acoustic field to achieve a controlled 2D motion of objects. An experimental platform containing an array of ultrasonic transducers was built, allowing for a non-contact manipulation with a plastic sphere floating on a water surface. To induce force on the sphere, the surrounding acoustic pressure field is shaped by controlling the phase shifts of the individual acoustic source elements. This work includes a description of the mechanical and electronic design of the set-up, the development of a control-oriented mathematical model of the system and the design of a feedback controller. Inside the controller block, a real-time optimization problem is solved every control period, providing a set of phase shifts corresponding to the required force. The control system is capable of steering the object of interest along a prescribed trajectory within the manipulation range of the platform. Both the trajectory tracking performance and the positioning accuracy were experimentally tested and analysed.

Keywords: ultrasound, non-contact manipulation, air-liquid interface, feedback control, real-time optimization

Supervisor: Ing. Tomáš Michálek

Abstrakt

Tato práce zkoumá využití akustického pole za účelem dosažení kontrolovaného dvourozměrného pohybu objektů. Byla postavena experimentální platforma s polem ultrazvukových měničů, jež umožňuje bezdotykově manipulovat s plastovou kuličkou plovoucí na vodní hladině. Pro vyvození síly se okolní pole akustického tlaku tvaruje pomocí řízení fázových posuvů jednotlivých akustických zdrojů. Tato práce obsahuje popis mechanického a elektronického návrhu, vývoje matematického modelu systému pro účely řízení a návrhu zpětnovazebního regulátoru. Uvnitř regulačního bloku se každou řídicí periodu řeší optimalizační úloha, která poskytuje sadu fázových posuvů, jež odpovídají požadované síle. Regulační systém je schopen řídit objekt po zadané trajektorii v rámci manipulačního dosahu platformy. Jak schopnost sledovat trajektorii, tak přesnost polohování byly experimentálně ověřeny a zanalyzovány.

Klíčová slova: ultrazvuk, bezkontaktní manipulace, rozhraní kapalina-vzduch, zpětnovazební řízení, optimalizace v reálném čase

Překlad názvu: Manipulace s objekty na hladině kapaliny pomocí pole ultrazvukových aktuátorů

Contents

Chapter 1

Introduction

The goal of the bachelor's project was to build an experimental platform and design a control algorithm for contactless ultrasonic manipulation with floating objects. The work was inspired by numerous papers on manipulation using acoustic [1, 2], electric [3] and magnetic [4] field, and should serve as an extension of the current portfolio of non-contact manipulation techniques investigated by the AA4CC research group of the Department of Control Engineering.

An overview of the state-of-the-art ultrasonic manipulation techniques is presented in the following section.

1.1 Other research

Regarding the use of ultrasound to manipulate objects, the most significant method is the acoustic levitation. This method utilizes acoustic pressure radiation force to counteract gravity. The phenomenon was first demonstrated in 1866 by August Kundt [5]. The first devices capable of levitating particles created static fields, which meant that they were able to suspend particles in mid-air but not to manipulate them.

In recent years, several acoustic levitation methods, which are capable of particle manipulation, have been developed. A comprehensive overview of

progress in acoustic levitation is given by Andrade *et al.* [6]. According to their paper, there are five types of acoustic levitation methods. Principles of their function are illustrated in Figure 1.1.

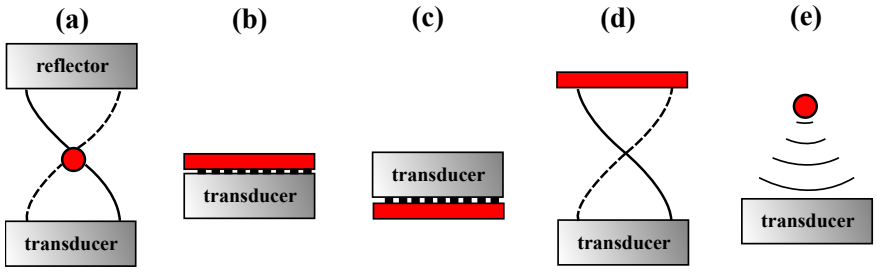

Figure 1.1: Schematic illustrations of different levitation methods. **a** Standing wave acoustic levitation. **b** Near-field acoustic levitation. **c** Ultrasonic suspension (inverse near-field acoustic levitation). **d** Far-field acoustic levitation. **e** Single beam acoustic levitation. (Redrawn from [6].)

In standing wave levitation, objects are trapped in pressure nodes of a standing wave (Figure 1.1 (a)). To manipulate with the objects, these pressure nodes must be movable, which can be achieved by positioning the reflector [7] or by replacing the transducer-reflector pair with one [8] or more [9] opposing pairs of phase controlled transducers. When travelling waves from two opposing transducers interfere, a standing wave is created. Changing the phase delay of the transducers alters the position of the standing wave nodes.

The near-field acoustic levitation method (Figure 1.1 (b)) is suitable for large planar objects. A standing wave is created with the object itself as a reflector. The reflector is subjected to acoustic radiation forces. These forces increase as the reflector approaches the transducer [10]. Therefore, the objects can levitate only in the vicinity of the transducer, where the forces are strong enough to counteract gravity. Manipulation can be achieved by using multiple transducers [11].

Similarly to near-field levitation, acoustic radiation forces act upwards even on objects placed under the transducer [12, 13] (Figure 1.1 (c)). Some articles refer to this as “ultrasonic suspension” [13] or “inverse near-field levitation” [6]. Recently, successful levitation of large objects further from the transducers was reported [14] (Figure 1.1 (d)). This method is referred to as “far-field levitation”.

Single beam levitation (Figure 1.1 (e)) is the only method which uses purely travelling waves. By controlling phase delays of a transducer array, it is possible to shape the surrounding acoustic field and create patterns which trap small (smaller than the wavelength) particles. Marzo *et al.* used

physical delay lines [15], or a custom made 64 channel generator [1] to control the phase delay of individual transducers. They were first to demonstrate successful single beam levitation using commercially available transducers[1].

Another interesting, rather artistic, application of ultrasound is "Ghost Touch" [2]. Analogically to single beam levitation, phase modulation is applied to a two-dimensional array of transducers to obtain focused ultrasound at an arbitrary position. Focused ultrasound can draw images on a thin layer of fine sand or sawdust (Figure 1.2a), create patterns with two immiscible liquids (Figure 1.2c), or make, move and pop bubbles on a soap solution (Figure 1.2b).

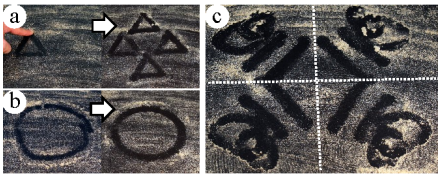

(a) : Effects of focused ultrasound on sawdust. Ghost Touch has several interactive functions. **a)** Copy and paste drawn images. **b)** Beautify drawn circles and lines. **c)** Mirroring. The top-left corner was drawn by the user. The remaining quadrants were made by Ghost Touch.

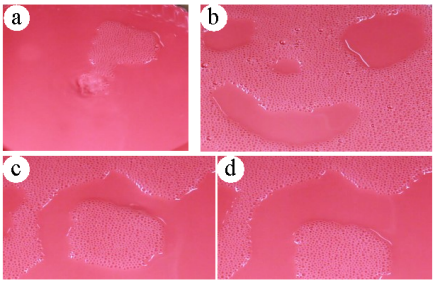

(b) : Effects of focused ultrasound on soap solution. **a)** Strong acoustic pressure generates bubbles. **b,c)** Medium pressure pops bubbles. **d)** Weak pressure can move bubbles.

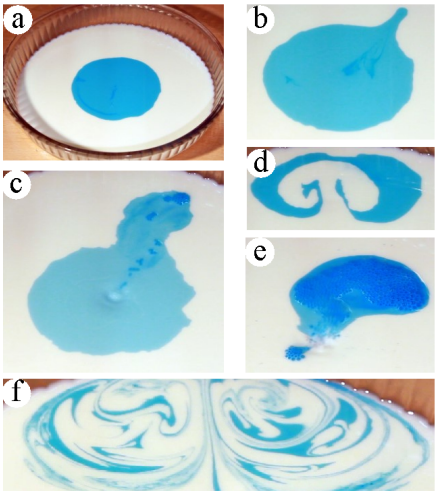

(c) : Effects of focused ultrasound on ink poured over milk. **a)** The original ink and milk blob. **b)** Weak acoustic pressure can drag thin strokes of ink. **c)** Medium pressure can drag thick strokes of ink. **d)** Medium-strong pressure can drag milk inside ink. **e)** Strong pressure can cause the blob to collapse or **f)** induce flow patterns.

Figure 1.2: Ghost Touch capabilities. (Reused from [2].)

[1] MA40S4S, Murata Electronics, Japan (see [1, Supplementary Materials] for more details)

1.2 Context

The bachelor's project is a continuation of work done throughout the summer internship at the AA4CC group and during the following winter semester in 2017. The initial intention was to replicate the results from one particular paper on acoustic levitation by Marzo *et al.* [1]. Therefore, the transducers used in this project are identical, and the eight-by-eight two-dimensional transducer array configuration is similar as well. During the winter semester within the Individual Project, the goal was to use focused ultrasound to shape the surface of a liquid, similarly to Ghost Touch [2] or a paper by Long *et al.* on rendering volumetric haptic shapes [16].

The physical model and the formulation of the optimization problem are also similar to those used in Ghost Touch. However, this thesis is unique in combining feedback control with ultrasonic manipulation, as very few papers on this subject exist. Courtney *et al.* state in their paper, that feedback or adaptive control could increase the precision of particle positioning [17]. They used a simple feedback control method, consisting of observing the position of the particles and manual adjustment, and thus no actual controller was designed. Furthermore, this project is unique in manipulation with floating particles (*i.e.*, particles on a liquid-fluid interface). Usually, ultrasonic manipulation is conducted on particles which are either on air [1, 8, 10–15], or fully submerged in liquid [9, 17].

Chapter 2

Experimental platform

Since this is a start-up project, a significant portion of the experimental platform had to be designed and built *from scratch*. This chapter describes mechanical and electronic components used in the platform. Since this experimental platform is used in a bachelor's thesis of my colleague, Adam Kollarčík, who deals with motion control on a solid surface, both of us took part in the design. Here, I will describe the components made solely by myself and will refer to the other thesis in the opposite cases.

2.1 Mechanical design

This section contains the description of mechanical components. Firstly, a list of required features is presented. Secondly, the mechanical solution meeting the requirements is described.

2.1.1 Requirements

The primary requirement posted on the mechanical design was to suspend an eight-by-eight two-dimensional array of ultrasonic transducers above an open container with floating objects.

Based on Marzo's work [1] and our observation, it was apparent that the maximum acoustic pressure increases with decreasing distance between the array and the object. However, due to the directivity of transducers, the active manipulation area in such case gets smaller. Increasing the distance has an opposite effect. At the beginning, it was unclear what the optimal height is, and thus the vertical position of the transducer array had to be adjustable.

Controlling the position of the objects utilizes optical feedback, which requires a camera. To avoid as much of unwanted image distortion as possible, it is advantageous to point the camera perpendicularly to the manipulation plane. Due to the obstructive array of transducers, we decided to place the camera underneath the tracked object and make the platform from transparent plexiglass.

Moreover, if the camera were placed at the height of the suspension, it would have to be pointed at an angle, which would distort dimensions in the picture. As the height of the array can be adjusted, the camera angle would have to be adjustable as well, in order to cover the whole manipulation area. It seems that placing the camera under the tracked object is the most straightforward solution.

2.1.2 Solution

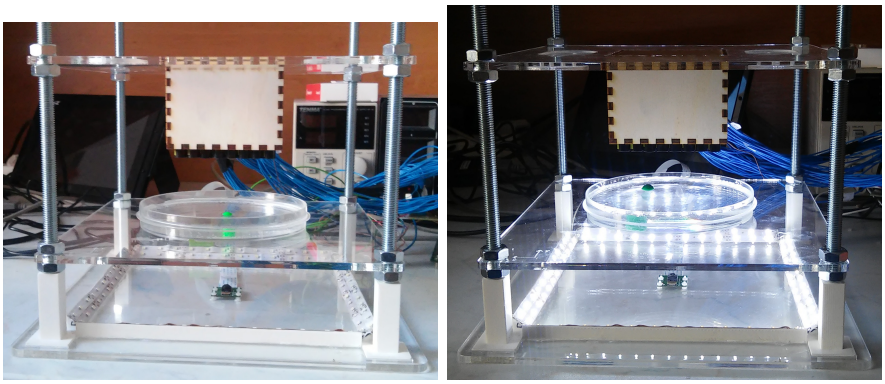

(a) : The platform with the lighting switched off.

(b) : The platform with the lighting switched on.

Figure 2.1: Photographs of the platform.

The platform consists of three transparent panes, as can be seen in Figure 2.1. Each pane was laser-cut from 5 mm thick plexiglass using the Epilog Mini 18 laser engraver.

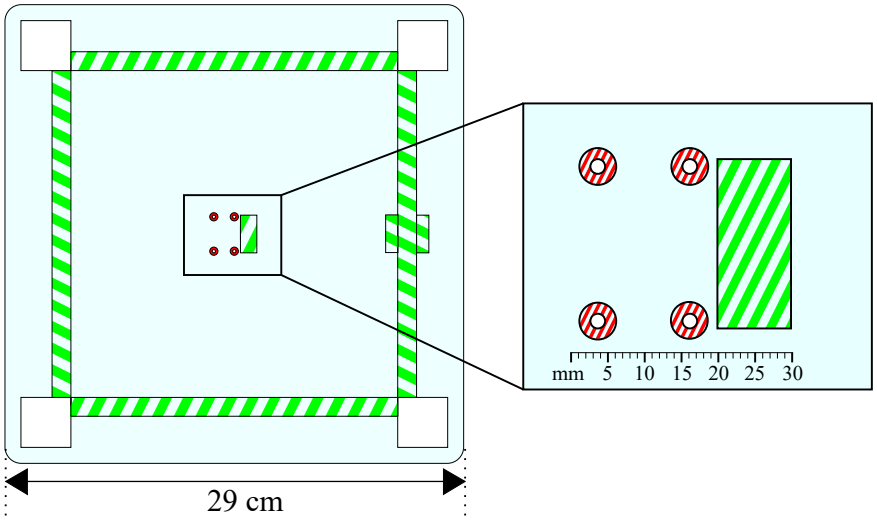

Figure 2.2: Drawing of the bottom pane. Green hatching represents top engraving; red hatching represents bottom engraving.

As can be seen in Figure 2.2, the bottom pane consists of a square with rounded edges having a side of 29 cm. In each corner of the pane is a 3 cm wide square cut-out. These cut-outs serve as a base for 3D-printed pillars. The pillars have a hole with an M10 thread inside, which allows screwing in a threaded rod serving as a support of the middle and the top pane.

Between the cut-outs for the pillars, there are rectangular engravings for fitting 3D-printed triangular prisms with LED stripes, which illuminate the platform. For more information on lighting, please refer to Adam Kollarčík's thesis [18].

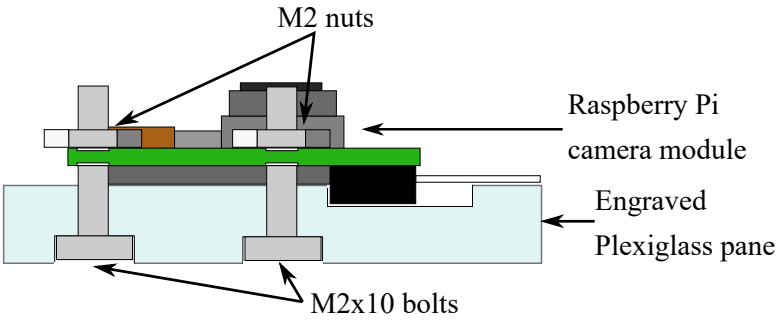

Figure 2.3: Side view of the bottom pane with the attached camera module

The engravings at the centre of the pane, shown in Figure 2.2, are used for attaching the Raspberry Pi camera module. The bottom engravings serve as sockets for the M2 bolts, while the top engraving makes space for a camera connector, and thus enables to level the module. A schematic illustration is shown in Figure 2.3.

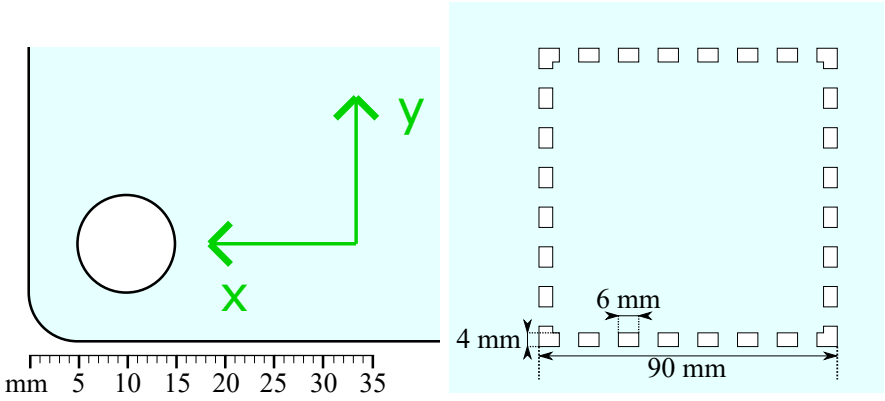

(a) : Detail of the middle pane's corner.

(b) : Detail of the top pane.

Figure 2.4: The middle and the top pane.

The middle pane is a 25 cm long sided square with rounded edges, and four circular cut-outs in its corners. An M10 threaded rod runs through each of these cut-outs. Four pairs of nuts placed under and above the pane suspend it at an arbitrary height. The middle pane supports the transparent container with the floating objects (as shown in Figure 2.1 with the Petri dish and the green ball). The only engraved feature here is the coordinate system, shown in Figure 2.4a. These coordinates are described in Chapter 3.

The top pane has the same dimensions as the middle pane and the same four circular cut-outs. In addition, there is a cut-out pattern at the centre, into which fits the transducer box. This pattern is shown in Figure 2.4b.

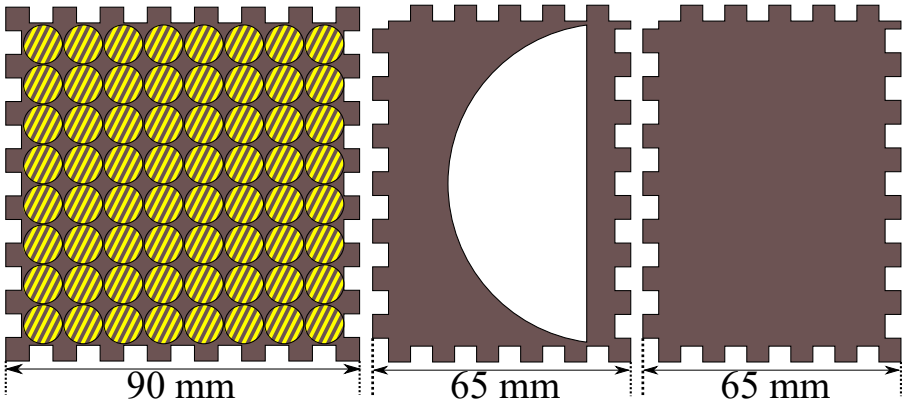

(a) : Bottom of the box with the transducers. Yellow hatching represents engraving.

(b) : Side of the box with a cut-out hole for the cables.

(c) : Side of the box with the transducers.

Figure 2.5: Drawings of the transducer box components.

The ultrasonic transducer array is placed at the bottom of a box made

from 4 mm thick plywood. The bottom of the box has 64 laser engraved circular pads, each with a pair of holes for contacts, as shown in Figure 2.5a. These pads provide housing for the transducers. In this arrangement, the contacts and wires are hidden inside the box for protection and isolation. The wires lead through a cut-out hole in one of the sides (Figure 2.5b). The three remaining sides are entirely solid (Figure 2.5c). The indented edges of the components form the so-called *finger joints*, which simplify the assembly. The free joints on the sides of the box are designed to fit into the cut-outs in the top plexiglass pane, which forms the top of the box.

2.2 Electronics

This section will cover the electronics used in the experimental set-up used for actuation, sensing and control action computation. A significant portion of the electronic design was already made during the summer internship in 2017 and throughout the following winter semester, within the Individual project. Namely, it was the printed circuit board with drivers powering the transducer array (used for the acoustic levitation at that time). In the following subsections, I will briefly describe this driver board and the rest of the relevant electronics.

2.2.1 Actuators

In this project, the Murata MA40S4S ultrasonic transducers are used. The most common applications of these transducers are distance measurement and obstacle detection, as the transducers function both as transmitters and receivers. However, in this project, they serve as ultrasonic emitters. The transducers are connected by crimping contacts. Individual wires lead from the positive terminals into 16-pin headers. The negative terminals are all connected to a single ground wire. The transducers are powered by 40 kHz square signal with a 16 V_{pp} amplitude. Due to the frequency characteristic of the transducers (narrow band-pass filter) [19], the higher harmonic components are filtered out, and the transducers emit a 40 kHz sine wave.

The device, which controls the transducers, must be capable of generating 64 square signals with individually configurable phase delays. Initially, a circuit board developed for the dielectrophoresis project was used [20]. Unfortunately, the board's outputs stage cannot provide sufficient current to power the

transducers. So, an additional circuit board with the Texas Instruments L293D drivers in half H-bridge configuration was made. The H-bridge board was designed to be attached on top of the generator board.

The generator communicates via RS-232. The communication protocol is in a simple text form, the commands are four letter words (see [21] for a list of commands and their usage). The communication script is written in the C programming language and is available in the materials on the supplementary CD of this thesis. The script is a modified version of the communication script used in the MagMan project[1].

During this semester, an undergraduate student, Petr Brož, was tasked to program a new 64 channel generator using the TerasIC DE0 Nano board. The new generator has better phase resolution (360 different phases compared to 16), and faster communication speed (up to 510 kBd compared to 19.2 kBd). Apart from the phase delay, the duty cycle of individual channels can be set as well. The DE0 Nano board has 3.3 V CMOS compatible outputs. To power the transducers, it requires the same additional driver board as the previously used generator.

The new generator communicates via UART. In the current state, it is possible to set the phase delays and duty cycles only; the frequency is fixed at 40 kHz. The process of setting the phase delays and duty cycles starts by sending a sequence of three bytes, `0xff`, `0xff`, `0xf0` in hexadecimal format. The phase delays and duty cycles are in 9-bit unsigned integer format, ranging from 0 to 360. The phase delay—duty cycle pairs are concatenated, then split into 8-bit packets and sent. The command ends with another three-byte sequence, `0xff`, `0xff`, `0xf1` in hexadecimal format. The communication script is written in C, and it is, like the script for the dielectrophoresis project generator, a modified version of the MagMan communication script.

2.2.2 Position measurement

The position of the manipulated object is measured by the Raspberry Pi camera module version 2. The script for determining the position of the object was made by my colleague, Adam Kollarčík [18]. He modified the *raspi-ballpos* script from the AA4CC group's GitHub[2] to obtain the position

[1] MagMan (Magnetic Manipulation) is a project researched by the AA4CC group, `http://aa4cc.dce.fel.cvut.cz/content/research`

[2] The *raspi-ballpos* script is available under the GPL-3.0 license, `https://github.com/aa4cc/raspi-ballpos`

of the object in the image and wrote a coordinate transform script to obtain the position in the coordinate system of the platform.

2.2.3 Control hardware

The Raspberry Pi 3 multimedia computer handles visual feedback control and communication with the generator board. The camera module is connected to the Raspberry Pi camera port via the standard ribbon cable. The generator is connected to the Raspberry Pi USB port via a USB-UART converter. The Raspberry Pi runs the *Raspbian Jesse* Linux distribution with a MATLAB server. The server allows to create the controller scheme in Simulink and then deploy it to the Raspberry. The scripts written in different programming languages can be added to Simulink using the MATLAB System Object interface.

Chapter 3

Modelling the acoustic pressure field

To evaluate forces acting on the floating object, we need to model the acoustic pressure field of the transducers. We neglect any reflections and model the acoustic pressure of a travelling wave. Although this model is not physically accurate, it is computable in real-time and sufficient for the purpose of control.

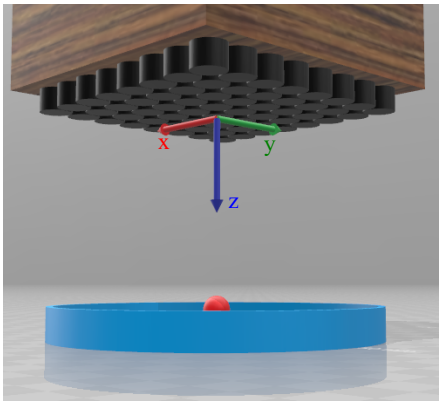

Figure 3.1: A 3D render of the platform with the indicated coordinate axes.

In the following chapters, unless noted otherwise, the coordinate system shown in Figure 3.1 will be used. The origin of the coordinate system is at the centre of the transducer array. The x-axis runs from right to left, the y-axis runs from front to rear, and the z-axis runs from top to bottom. Therefore, the coordinate system is right-handed.

When calculating the overall acoustic pressure, we assume the principle of superposition. For the overall pressure $\tilde{p}$ at a point with coordinates (x, y, z), and the number of transducers N, we obtain

$$\tilde{p}(x, y, z) = \sum_{i=1}^{N} \tilde{p}_i(x, y, z), \tag{3.1}$$

where $\tilde{p}_i$ is the acoustic pressure contribution from the i^{th} transducer. A phasor notation ($\tilde{p}$) is used here. The acoustic pressure p at a given time t

can be expressed as

$$p(x, y, z, t) = \mathfrak{Re}\left\{\tilde{p}(x, y, z)\mathrm{e}^{j\omega t}\right\}, \tag{3.2}$$

where ω is the angular frequency, $\mathfrak{Re}\{.\}$ denotes the real part of a complex number, and $j = \sqrt{-1}$ is the imaginary unit. As we are only interested in the amplitude of acoustic pressure, the formulae do not need to include the time.

In literature, there are different methods how to model the acoustic pressure field of an ultrasonic piezoelectric transducer.

3.1 Model from the Ghost Touch

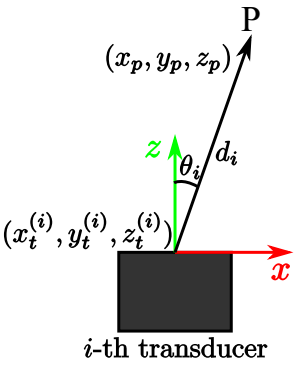

Figure 3.2: A sketch of the distance and the angle from the i^{th} transducer.

In the paper on Ghost Touch [2], the acoustic pressure contribution from the i^{th} transducer is expressed as

$$p_i = M_i \mathrm{e}^{j\varphi_i}, \tag{3.3}$$

where φ_i is the phase delay, and M_i is a complex constant given by

$$M_i = A f_{\text{dir}}(\theta_i) \frac{1}{d_i} \mathrm{e}^{jkd_i}, \tag{3.4}$$

where A is the power of the transducer, f_{dir} is the so-called directivity function representing the polar pattern of the transducer, k is the wavenumber, d_i is the distance from the i^{th} transducer, and θ_i is the angle between the axis of the transducer and the transducer-point connector. The distance and the angle are shown in Figure 3.2.

The position of both the transducers and the evaluated point is in (x, y, z) coordinates. Therefore, we need to express the distance and angle using these coordinates. In the aforementioned coordinate system, the axes of the transducers are parallel to the z-axis, and all transducers have their z-coordinate equal to zero. When evaluating the acoustic pressure at a point P with coordinates $(x_{\text{P}}, y_{\text{P}}, z_{\text{P}})$ from the i^{th} transducer with coordinates $(x_{t_i}, y_{t_i}, z_{t_i})$, the distance d_i, thanks to $z_{t_i} = 0$, is

$$d_i = \sqrt{(x_{\text{P}} - x_{t_i})^2 + (y_{\text{P}} - y_{t_i})^2 + {z_{\text{P}}}^2}, \tag{3.5}$$

and the sine and cosine of the angle θ_i is

$$\sin\theta_i = \sqrt{\frac{(x_\mathrm{P}-x_{t_i})^2+(y_\mathrm{P}-y_{t_i})^2}{(x_\mathrm{P}-x_{t_i})^2+(y_\mathrm{P}-y_{t_i})^2+{z_\mathrm{P}}^2}} = \frac{\sqrt{(x_\mathrm{P}-x_{t_i})^2+(y_\mathrm{P}-y_{t_i})^2}}{d_i}, \tag{3.6a}$$

$$\cos\theta_i = \frac{z_\mathrm{P}}{\sqrt{(x_\mathrm{P}-x_{t_i})^2+(y_\mathrm{P}-y_{t_i})^2+{z_\mathrm{P}}^2}} = \frac{z_\mathrm{P}}{d_i}. \tag{3.6b}$$

The directivity function f_dir depends on the angle θ_i. It represents attenuation, and thus its absolute value should fall in the unit interval. From higher angles, some transducers emit a wave with phase shifted by π radians. Therefore, the directivity function can attain negative values as well. The directivity function can be obtained from the manufacturer's specifications.

3.2 Piston source model

Another approach is to model the vibrating membrane of the transducer as a piston source. In the textbook *Fundamentals of Acoustics* by Kinsler *et al.*, a formula describing the far-field[1] of a circular piston source is derived [22, p. 179-182]. The equation has been rewritten to comply with the previous notation

$$M_i = \frac{j}{2}\rho_0 c U_0 k r^2 \left[\frac{2J_1(kr\sin\theta_i)}{kr\sin\theta_i}\right]\frac{1}{d_i}\mathrm{e}^{-jkd_i}, \tag{3.7}$$

where ρ_0 is the air density, c is the speed of sound, U_0 is the amplitude of velocity of the piston, k is the wavenumber, r is the radius of the piston, J_1 is the first-order Bessel function of the first kind, d_i and θ_i is the distance and angle described in the previous section, respectively.

3.3 Comparison

Immediately, we can see some similarities between the models described by Equations 3.4 and 3.7. The term $\frac{1}{2}\rho_0 c U_0 k r^2$ is a real constant, and can be interpreted as the power of the transducer, A. The imaginary unit can

[1] In far-field, the distance from the transducer $d_i \gg r$, where r is the radius of the transducer.

be interpreted as a phase shift, which does not affect the overall pressure amplitude, and thus can be omitted. The bracketed term has the properties of the directivity function. Although its value for $\theta_i = 0$ is not defined, it has a limit at that point equal to one. The comparison between the directivity function of the piston source model and the manufacturer's specifications is shown in Figure 3.3.

The term $\frac{1}{d_i}$ is identical in both formulae. The exponents of the exponentials have opposite signs, which seems like a contradiction. However, in our phasor notation, it is only a matter of choice, whether the phasors rotate in clockwise or anti-clockwise direction.

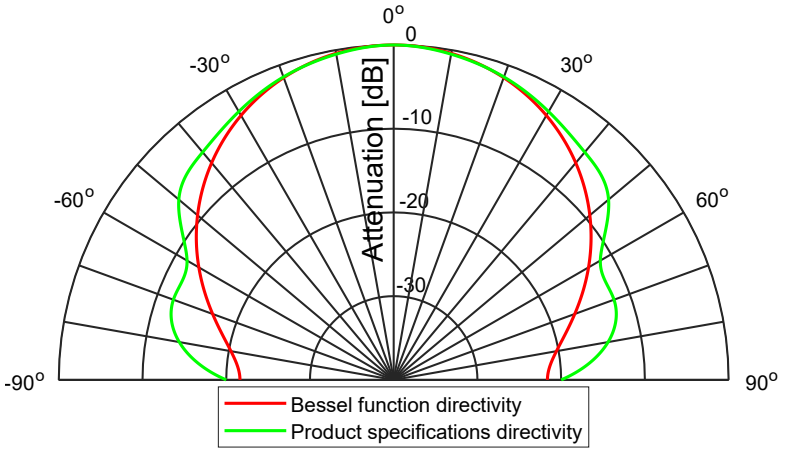

Figure 3.3: Comparison between the directivity functions. Manufacturer's specifications obtained from [19].

3.4 The model used in this thesis

In this thesis, we use the Ghost Touch model with the directivity function extracted from the piston source model

$$M_i = A\frac{2J_1(kr\sin\theta_i)}{kr\sin\theta_i}\frac{1}{d_i}\mathrm{e}^{jkd_i}. \tag{3.8}$$

We cannot determine the power of the transducers, A, from the piston source model, because some constants, such as the amplitude of velocity, are impossible to measure. Instead, we take the necessary information from the manufacturer's specifications. The sound pressure level at 25 cm distance from the transducer, directly on its axis, is 120 dB [19], which is equivalent to the acoustic pressure of 20 Pa. From (3.4) (with directivity equal to one), we obtain the power of the transducer, $A = 5\,\mathrm{Pa\,m}$.

Chapter 4

Inversion of the acoustic pressure model

Regardless of the specific technique for controlling the motion of the floating object (pushing the object, trapping the object *etc.*), the fundamental actuation principle is always the same — creating an area of high acoustic pressure, which forces the manipulated object to move to a lower pressure zone. In the previous chapter, we obtained a formula for the acoustic pressure at any given point and a given set of phase delays. Now, we have a prescribed acoustic field, and we need to find the corresponding phase delays of the individual transducers. To obtain the phase delays, we formulate an optimization problem. Suppose there are L points in space, where we require acoustic pressure amplitudes $P_1, P_2, \ldots, P_L$. Then, the criterion function $\mathcal{O}$ of the phase delays of individual transducers, $\varphi_1, \varphi_2, \cdots, \varphi_N$, is

$$\mathcal{O}(\varphi_1, \varphi_2, \ldots, \varphi_N) = \sum_{k=1}^{L} \left(\left| \tilde{p}^{(k)} \right| - P_k \right)^2, \tag{4.1}$$

where $\tilde{p}^{(k)}$ is the complex acoustic pressure at the k^{th} point, computed from (3.1). The optimal phase delays are:

$$(\varphi_1, \varphi_2, \ldots, \varphi_N) = \phi = \underset{\phi \in \mathbb{R}^N}{\arg\min}\, \mathcal{O}(\phi) \tag{4.2}$$

To solve this problem, we use the BFGS optimization algorithm. This algorithm requires the gradient of the criterion function as an input

$$\nabla \mathcal{O} = \left(\frac{\partial \mathcal{O}}{\partial \varphi_1}, \frac{\partial \mathcal{O}}{\partial \varphi_2}, \cdots, \frac{\partial \mathcal{O}}{\partial \varphi_N} \right). \tag{4.3}$$

The partial derivative of the criterion function with respect to the phase

delay of the i^{th} transducer is:

$$\frac{\partial \mathcal{O}}{\partial \varphi_i} = \sum_{k=1}^{M} \left(\left| \tilde{p}^{(k)} \right| - P_k \right) \frac{\partial \left| \tilde{p}^{(k)} \right|}{\partial \varphi_i}. \tag{4.4}$$

Now, we need to express the absolute value of the acoustic pressure in terms of the phase delays. Let us start with the square of the absolute value, which is equal to the product of the overall acoustic pressure and its complex conjugate. Substituting from (3.3), we obtain

$$\left| \tilde{p}^{(k)} \right|^2 = \left(\sum_{i=1}^{N} M_i^{(k)} \mathrm{e}^{j\varphi_i} \right) \left(\sum_{i=1}^{N} \overline{M_i^{(k)}} \mathrm{e}^{-j\varphi_i} \right). \tag{4.5}$$

Now, its partial derivative

$$\frac{\partial}{\partial \varphi_i} \left| \tilde{p}^{(k)} \right|^2 = j M_i^{(k)} \mathrm{e}^{j\varphi_i} \left(\sum_{i=1}^{N} \overline{M_i^{(k)}} \mathrm{e}^{-j\varphi_i} \right) - j \overline{M_i^{(k)}} \mathrm{e}^{-j\varphi_i} \left(\sum_{i=1}^{N} M_i^{(k)} \mathrm{e}^{j\varphi_i} \right), \tag{4.6}$$

into which we now substitute $p_i^{(k)}$ as $M_i^{(k)} \mathrm{e}^{j\varphi_i}$, and $\tilde{p}^{(k)}$ as $\sum_{i=1}^{N} M_i^{(k)} \mathrm{e}^{j\varphi_i}$:

$$\frac{\partial}{\partial \varphi_i} \left| \tilde{p}^{(k)} \right|^2 = j p_i^{(k)} \overline{\tilde{p}^{(k)}} - j \overline{p_i^{(k)}} \tilde{p}^{(k)}. \tag{4.7}$$

Now, we express the complex pressures with their real and imaginary parts

$$\begin{aligned} \frac{\partial}{\partial \varphi_i} \left| \tilde{p}^{(k)} \right|^2 = {} & j \left(\mathfrak{Re}\left\{ p_i^{(k)} \right\} + j \mathfrak{Im}\left\{ p_i^{(k)} \right\} \right) \left(\mathfrak{Re}\left\{ \tilde{p}^{(k)} \right\} - j \mathfrak{Im}\left\{ \tilde{p}^{(k)} \right\} \right) \\ & - j \left(\mathfrak{Re}\left\{ p_i^{(k)} \right\} - j \mathfrak{Im}\left\{ p_i^{(k)} \right\} \right) \left(\mathfrak{Re}\left\{ \tilde{p}^{(k)} \right\} + j \mathfrak{Im}\left\{ \tilde{p}^{(k)} \right\} \right). \end{aligned} \tag{4.8}$$

Following some simplifications, we obtain

$$\frac{\partial}{\partial \varphi_i} \left| \tilde{p}^{(k)} \right|^2 = 2 \mathfrak{Im}\left\{ \tilde{p}^{(k)} \right\} \mathfrak{Re}\left\{ p_i^{(k)} \right\} - 2 \mathfrak{Im}\left\{ p_i^{(k)} \right\} \mathfrak{Re}\left\{ \tilde{p}^{(k)} \right\}. \tag{4.9}$$

For the partial derivative, the following must hold true as well

$$\frac{\partial}{\partial \varphi_i} \left| \tilde{p}^{(k)} \right|^2 = 2 \left| \tilde{p}^{(k)} \right| \frac{\partial \left| \tilde{p}^{(k)} \right|}{\partial \varphi_i}. \tag{4.10}$$

Combining the two previous equations, we finally obtain

$$\frac{\partial \left| \tilde{p}^{(k)} \right|}{\partial \varphi_i} = \left(\mathfrak{Im}\left\{ \tilde{p}^{(k)} \right\} \mathfrak{Re}\left\{ p_i^{(k)} \right\} - \mathfrak{Im}\left\{ p_i^{(k)} \right\} \mathfrak{Re}\left\{ \tilde{p}^{(k)} \right\} \right) \frac{1}{\left| \tilde{p}^{(k)} \right|}, \tag{4.11}$$

which can be substituted back into (4.4).

4.1 Implementation

The optimization algorithm is implemented in C++, using the *L-BFGS++* solver[1] rather than the standard BFGS. Unlike BFGS, which stores the dense approximation of the inverse Hessian, the L-BFGS stores only a few gradients from the previous steps, from which it calculates the inverse Hessian approximation. For vector and matrix operations, the *Eigen* linear algebra library[2] is used.

In addition to these libraries, the acoustic pressure formula from Chapter 3, and the objective function and its gradient from this chapter had to be implemented. All source codes are available in the materials on the supplementary CD of this thesis.

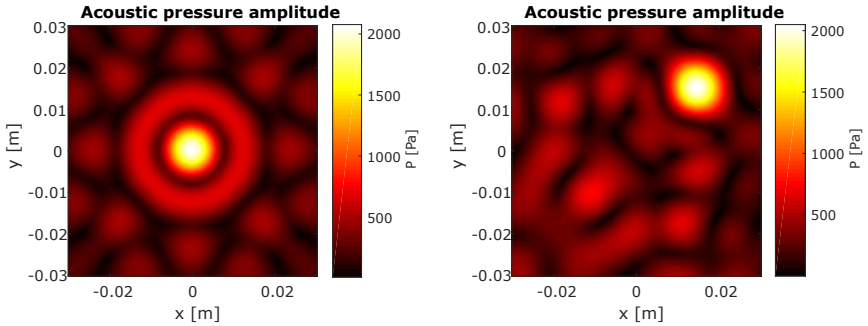

(a) : Required amplitude 2000 Pa at (0,0,65) mm.

(b) : Required amplitude 2000 Pa at (15,15,65) mm.

Figure 4.1: 2D slice of the 3D acoustic pressure field emitted by the transducers with phase delays obtained from the optimization algorithm. The slice plane is horizontal located at $z = 65$ mm underneath the transducer array.

The results of the optimization algorithm are shown in Figure 4.1. We can see that specifying the same amplitude of pressure at different coordinates produces similarly shaped acoustic fields.

The initial conditions of the optimization algorithm have a significant influence on the resulting acoustic field. The resulting phase delays from Figure 4.1 were initiated from zeros (the so-called "cold start" method). When an optimization algorithm is run repetitively with only small changes in criterion, it may be advantageous to initiate the algorithm from the result of the previous run, since the optimal value is likely to be close and a significant number of solver iterations can be saved. This is called the "warm start"

[1] *LBFGS++* is an open source project under the MIT license, `https://yixuan.cos.name/LBFGSpp/`

[2] *Eigen* is free software under the MPL2 license, `http://eigen.tuxfamily.org/`

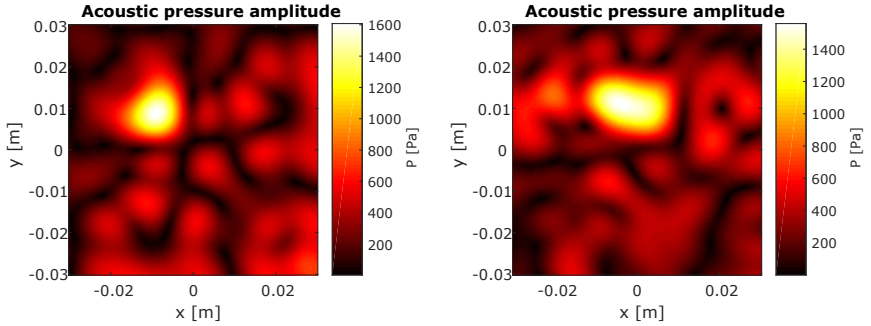

(a) : Initial condition. **(b) :** Resulting phase delays.

Figure 4.2: Demonstration of the "warm start" method.

method. Figure 4.2 shows the result of the "warm start" method. The resulting high-pressure area is wider than the high-pressure areas initiated using the "cold start" method. This can result in unexpected behaviour of the manipulated object, as we usually need a "sharp" high-pressure point. Therefore, we will use the "cold start" method only.

Chapter 5

Modelling the movement of a floating sphere

To design a motion controller for objects floating on a surface of a liquid, it is necessary to create a mathematical model including all the relevant physical phenomena. In our case, the object is subjected to two major forces, the force of the acoustic field, and the drag (friction) force of the liquid. Obviously, there are more phenomena, such as the capillary forces between the floating object and the walls of the container. These forces can be significantly reduced by using larger containers, as the capillary forces decrease with the square of the distance. Furthermore, there is the effect of the acoustic field on the liquid. Focused ultrasound can shape the surface of the liquid, create waves and even bubbles as a result of cavitation. These phenomena affect the floating object, but are difficult to predict and model. We will rely on the robustness of the feedback controller and its ability to overcome these forces.

The model described in this chapter is suitable for spherical floating objects. When modelling the object, we assume the vertical forces to be in equilibrium. Then, we decouple the movement into x- and y- components. We do not need to model the motion of the object in the z-coordinate, since its position is given by the level of the liquid. The object is subjected to drag force $\mathbf{F}_{\mathrm{D}} = (F_{\mathrm{D}x}, F_{\mathrm{D}y}, 0)$, and external force $\mathbf{F} = (F_x, F_y, 0)$ caused by the acoustic field. Applying Newton's second law, we obtain

$$m\ddot{x} = F_{\mathrm{D}x} + F_x, \tag{5.1a}$$
$$m\ddot{y} = F_{\mathrm{D}y} + F_y, \tag{5.1b}$$

where x and y are the coordinates, and m is the mass of the object.

5.1 Modelling the drag

A simple, yet frequently used method how to model the drag force of a floating sphere is the modified Stokes' law [23–25]

$$F_{\mathrm{D}x} = -6\pi\beta R\mu\dot{x}, \tag{5.2}$$

where R is the radius of the sphere, μ is the dynamic viscosity of the liquid, and β is a correction constant. For the y-component of the drag force, the equation is similar.

For $\beta = 1$, the Equation (5.2) is identical to the original well-known Stokes' law, which applies to fully submerged objects only. However, it has been experimentally found, that drag force acting on floating objects has the same order of magnitude as the Stokes' drag force [24, 25]. Nevertheless, we will have to utilize the system identification techniques to obtain the value of β for our case (as will be described in detail in Section 5.3).

5.2 Dependence of the applied force on the acoustic pressure field

Apart from the unknown coefficient of drag, it is necessary to obtain an equation relating the acoustic pressure and the force, by which it acts on the object. The subject of modelling the forces arising from the acoustic field, the so-called acoustic pressure radiation forces, is complicated. King derived a formula for the acoustic pressure radiation force acting on spheres [26]. However, it is only applicable to axially symmetrical acoustic fields, and while the acoustic field of a single transducer is symmetrical, the acoustic field of the entire array of transducers is not.

Another formula was devised by Gor'kov (because the original article is in Russian and the English translation is difficult to obtain, we cite an article by Bruus [27] on the same topic). In his approach, the acoustic field does not need to be symmetrical. However, the particles subjected to the acoustic pressure radiation force must be significantly smaller than the wavelength. Although this requirement is not met[1], the observed forces (or at least their direction) match the forces predicted by Gor'kov's model.

[1] In the experiments, polypropylene balls with 8 mm in diameter were used, while the wavelength is approximately 8.5 mm

In Gor'kov's model, the acoustic pressure radiation force is

$$\mathbf{F} = -\nabla\left(U + V\right), \tag{5.3}$$

where U is the acoustic pressure potential, and V is the acoustic velocity potential. The potentials can be expressed as

$$U = K_1|\tilde{p}|^2, \quad V = K_2|\mathbf{v}|^2, \tag{5.4}$$

where $\tilde{p}$ is the phasor of the acoustic pressure, $\mathbf{v}$ is the acoustic velocity, and K_1 and K_2 are constants depending on the size of the particle, and the density and speed of sound in both the particle and the carrier medium.

There are two possible ways to manipulate objects using the acoustic pressure radiation force. One way is to create a sink in the radiation force field by minimizing the divergence of the force at the given point (which is, due to the Equation (5.3), equivalent to maximizing the Laplacian of the potentials). If the manipulated object is in the vicinity of the sink, it is attracted towards it. This method is used in single beam levitation by Marzo *et al.* [1]. However, larger particles become unstable and are cast out from the sink. Therefore, this method is not suitable for our application.

The other way is to specify the force by optimizing the gradient of the potentials. To obtain this gradient, the spatial derivatives of the acoustic pressure would have to be evaluated, which takes too much computational time. Instead, we use a more straightforward solution. According to the paper on acoustic levitation by Marzo *et al.*, the gradient of the acoustic pressure potential in horizontal direction is greater than the gradient of the acoustic velocity potential [1]. Therefore, we can neglect the acoustic velocity potential and model the acoustic radiation force as

$$\mathbf{F} = -K_1\nabla|\tilde{p}|^2. \tag{5.5}$$

By specifying the optimization problem from Chapter 4 with a high-pressure point on the edge of the object, and a zero-pressure point at the centre of the object, a steep gradient of acoustic pressure is assured, and the acoustic pressure radiation force pushes the object away from the high-pressure point. Now, we need to find the dependence of the resulting force on the high-pressure point amplitude. According to (5.5), the dependence should be linear. However, the particle in our experiments does not move, until the high-pressure amplitude exceeds a certain threshold. Because the output of our controller is the required force, it is convenient to find the dependence in the following form

$$P = |\mathbf{F}|P_{\text{lin}} + P_{\text{off}}, \tag{5.6}$$

where P is the required pressure amplitude (as shown in Chapter 4), P_{lin} is the linear coefficient, and P_{off} is a constant offset.

5.3 Identifying the parameters

Let $b = 6\pi\beta R\mu$. Substituting (5.2) into (5.1a), we obtain

$$m\ddot{x} + b\dot{x} = F_x. \tag{5.7}$$

Applying Laplace transform to the equation, we obtain transfer function from lateral force to position

$$\frac{x(s)}{F_x(s)} = \frac{1}{ms^2 + bs}. \tag{5.8}$$

Therefore, it is possible to get the parameter b by estimating the measured position of the floating object as a second order linear system. The coefficient from the Stokes' law serves as a verification that the estimated parameter has the correct order of magnitude.

Both the drag coefficient and the force to pressure conversion constants can be identified with one type of experiment. In the experiment, the floating object is subjected to a short pulse of high acoustic pressure. Then, the transducer array shuts down, and we measure the response of the object. We add the acoustic pressure as input and use the MATLAB System Identification Toolbox to identify the transfer function of the model. The estimated transfer function $\widehat{H}(s)$ will have the following form

$$\widehat{H}(s) = \frac{\widehat{a}}{s^2 + \widehat{b}s + \widehat{c}}, \tag{5.9}$$

where $\widehat{a}$ is the estimated numerator, $\widehat{b}$ and $\widehat{c}$ are the linear and constant coefficients of the estimated denominator. The estimated parameter $\widehat{c}$ should be small (ideally zero) to match the model from (5.8). The coefficient of drag b and the estimated parameter $\widehat{b}$ are in the following relation

$$b = m\widehat{b}, \tag{5.10}$$

where m is the mass of the object. As mentioned above, the input in the estimated transfer function is the acoustic pressure amplitude. Combining (5.8) and (5.9), we obtain the relation between the estimated force $\widehat{F}$ and the amplitude of the acoustic pressure pulse P

$$\widehat{F} = mP\widehat{a}. \tag{5.11}$$

When we group the experiments with the same pressure amplitude and identify the parameters, we get a set of estimated forces corresponding to acoustic pressure amplitudes. Interpolating the results with a linear function, we obtain the constants P_{lin} and P_{off}. Twelve sets of experiments with acoustic

pressure amplitudes varying from 1000 Pa to 2750 Pa were conducted. The manipulated object was a polypropylene sphere with 8 mm in diameter and a mass of 0.23 g. The results of the identification are shown in Table 5.1.

No. of experiment	P [Pa]	$\widehat{b}$ [s^{-1}]	$\widehat{F}$ [µN]
1	1250	2.29	2.71
2	1500	2.39	4.71
3	1750	3.23	10.38
4	2000	2.98	10.88
5	2250	4.37	17.95
6	2500	3.37	12.80
7	2750	0.93	12.26
8	1000	0.32	0.73
9	1250	1.11	5.95
10	1500	0.58	4.29
11	1750	0.90	10.90
12	2000	0.67	5.88

Table 5.1: Parameters identified from the experiments.

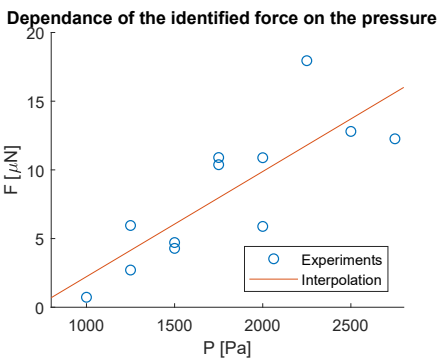

(a) : Dependence of the identified force on the acoustic pressure amplitude.

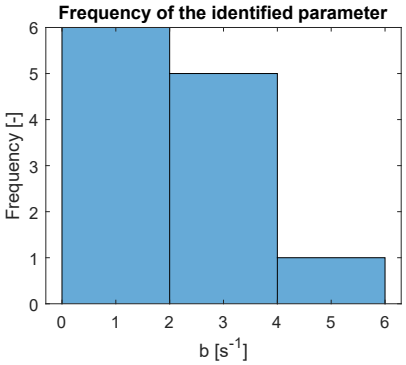

(b) : Histogram of the identified $\widehat{b}$ parameter's frequency.

Figure 5.1: Visualized results of the identification

Figure 5.1a shows the dependence of the identified force on the acoustic pressure amplitude. We use the least squares method to interpolate the force-pressure dependence. The linear coefficient is $P_{\text{lin}} = 1.31 \times 10^8\,\text{Pa}\,\text{N}^{-1}$, the constant offset is $P_{\text{off}} = 709\,\text{Pa}$. The distribution of the identified parameter $\widehat{b}$ is shown in Figure 5.1b. The mean of the parameter is $1.93\,\text{s}^{-1}$. Substituting to (5.10), we obtain the drag force coefficient $b = 4.44 \times 10^{-4}\,\text{N}\,\text{s}\,\text{m}^{-1}$. The coefficient from the Stokes' law is equal to $7.54 \times 10^{-5}\,\text{N}\,\text{s}\,\text{m}^{-1}$, which is almost by order of magnitude smaller. It is therefore questionable, whether the measured coefficient is correct, as it should probably be smaller. This uncertainty can be solved by designing a robust controller.

Chapter 6

Controller design

The model from the previous chapter is not complete, because the system is also affected by propagation delay. There is an approximately 20 ms long delay caused by the computation of the control action, the optimization problem, and communication with the generator; and another 60 ms delay caused by processing the image from the camera. The framerate of the camera is 50 Hz, which limits the minimum length of the simulation step to 20 ms. With the shortest possible simulation step, the total propagation delay corresponds to four simulation steps.

The propagation delay can be compensated by discretising the model from the previous chapter. Let $\mathbf{A}$, $\mathbf{B}$, and $\mathbf{C}$ be matrices of the second order discretised system (with no propagation delay), so that:

$$\mathbf{x}_{n+1} = \mathbf{A}\mathbf{x}_n + \mathbf{B}u_n, \tag{6.1a}$$

$$y_n = \mathbf{C}\mathbf{x}_n, \tag{6.1b}$$

where $\mathbf{x}_n$ is a vector of the discretised states, y_n is the discretised output (equivalent to position), u_n is the discretised input (equivalent to force), and n is the current discrete step. The matrices can be chosen to have one of the states equal to the output. Without loss in generality (as we can swap the states), let the second state be equal to the output. Thus the matrix $\mathbf{C} = \begin{pmatrix} 0 & 1 \end{pmatrix}$.

Now, we can add four-step delay to the model by adding four states. For the extended state matrix $\bar{\mathbf{A}}$, and extended input matrix $\bar{\mathbf{B}}$, the following

holds true:

$$\bar{\mathbf{A}} = \left(\begin{array}{cc|cccc} & \mathbf{A} & 0 & 0 & 0 & 0 \\ & & 0 & 0 & 0 & 0 \\ \hline 0 & 1 & 0 & 0 & 0 & 0 \\ 0 & 0 & 1 & 0 & 0 & 0 \\ 0 & 0 & 0 & 1 & 0 & 0 \\ 0 & 0 & 0 & 0 & 1 & 0 \end{array}\right), \quad \bar{\mathbf{B}} = \begin{pmatrix} \mathbf{B} \\ \mathbf{O} \end{pmatrix}. \tag{6.2}$$

Now, the model includes both the delayed and undelayed output. Let us denote the delayed output matrix $\mathbf{C}_{\text{del}}$ and the undelayed output matrix $\mathbf{C}_{\text{und}}$. These matrices are:

$$\mathbf{C}_{\text{del}} = \begin{pmatrix} 0 & 0 & 0 & 0 & 0 & 1 \end{pmatrix}, \quad \mathbf{C}_{\text{und}} = \begin{pmatrix} 0 & 1 & 0 & 0 & 0 & 0 \end{pmatrix}. \tag{6.3}$$

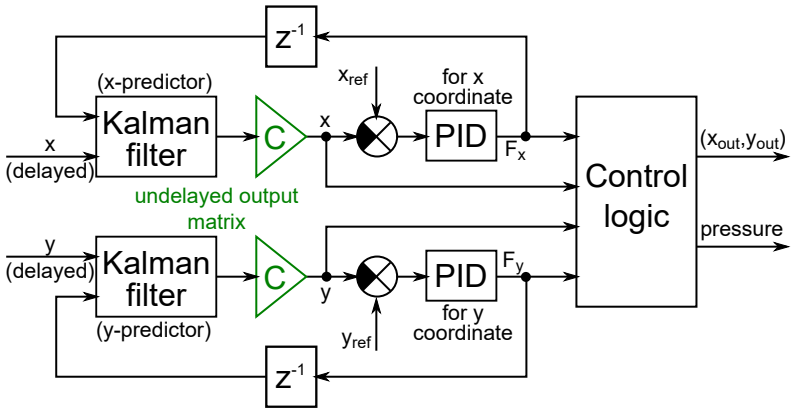

Figure 6.1: Signal flowchart of the controller

In the controller, we use a Kalman filter to compensate the delay. The discrete state-space matrices used in the model of the filter are $\bar{\mathbf{A}}$, $\bar{\mathbf{B}}$, $\mathbf{C}_{\text{del}}$, and zero as the feedforward matrix. The estimated states are then multiplied by $\mathbf{C}_{\text{und}}$ to obtain the predicted position. The position is then subtracted from the reference and sent to the PID controller to compute the required force. The force is fed back to the filter with a one simulation step long delay (represented by the z^{-1} block) to eliminate algebraic loops and simultaneously sent together with the estimated position to the "Control logic" script, which calculates the required position of the high-pressure point and its amplitude. A signal flowchart of the controller is shown in Figure 6.1.

We used the MATLAB PID Tuner application to get the constants of the controller. Due to the uncertainty in the model, we specified maximum robustness and obtained two sets of constants for two different settling times of 15 and 5 seconds. In the following text, we denote the resulting controllers as "version 1" and "version 2", respectively. The constants of the PID controller are shown in Table 6.1.

PID constants	K_P $[\mathrm{N\,m^{-1}}]$	K_I $[\mathrm{N\,m^{-1}\,s^{-1}}]$	K_D $[\mathrm{N\,s\,m^{-1}}]$
Version 1	5.1×10^{-4}	7.1×10^{-5}	4.1×10^{-4}
Version 2	4.9×10^{-3}	2.4×10^{-3}	2.6×10^{-3}

Table 6.1: Constants of the PID controller

It is also necessary to limit the output of the controller, as amplitudes of pressure above 2500 Pa create bubbles in the liquid. Using (5.6), we compute the output saturation, F_sat:

$$|F_\mathrm{sat}| = \frac{2500\,\mathrm{Pa} - P_\mathrm{off}}{P_\mathrm{lin}} = 1.3 \times 10^{-5}\,\mathrm{N}. \tag{6.4}$$

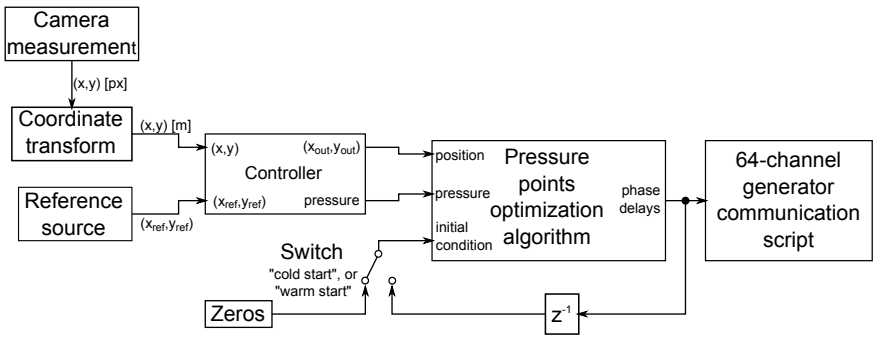

Figure 6.2: Block diagram of the control scheme

The whole control scheme is shown in Figure 6.2. Most of its blocks were described in previous chapters. For the "Reference Source", we use either a "Constant" block to stabilize the object in a specific position or a "Repeating Sequence" block to track a predefined trajectory. The z^{-1} block is a unit delay. The initial condition of the optimization algorithm can be switched to zeros ("cold start"), or the phase delays from the previous step ("warm start"). The difference between them is demonstrated in Chapter 4. In the experiments, we use the "cold start" method.

The Simulink control scheme is available in the supplementary materials in two versions, with or without the Kalman filter. The PID controller constants can be changed in the MATLAB workspace or by modifying the pre-load function in the Simulink Model Parameters.

Chapter 7

Evaluating the results

In this chapter, the results of experiments with the designed controllers are evaluated. We compare the data measured on the experimental platform to simulations, demonstrate how the compensation of propagation delay using the Kalman filter improves the behaviour of the controller, and present the ability of the controller to follow a prescribed trajectory.

7.1 Response to the change of reference

Firstly, we compare the two sets of PID controller constants shown in Table 6.1. We abbreviate the "PID version 1" and "PID version 2" controllers to "PID v1" and "PID v2", respectively. *PID v1* is tuned to have a settling time of 15 seconds and 15 % overshoot. *PID v2* has a faster settling time of 5 seconds at the cost of greater overshoot of 25 %.

The comparison of these two controllers, both on the real system and in the simulation, is shown in Figure 7.1. Both controllers utilize the propagation delay compensator. In the experiment, *PID v1* settles faster than the simulation predicts, but it also undershoots. The longer settling time of *PID v2*, both in the experiment and in the simulation, is caused by the saturation. The overshoot in the experiment is significantly smaller than in the simulation, while the rise time is longer. This could be caused by non-linearity of the drag force at higher velocities. In the experiment, the manipulated particle exhibits small oscillations, which indicates that the

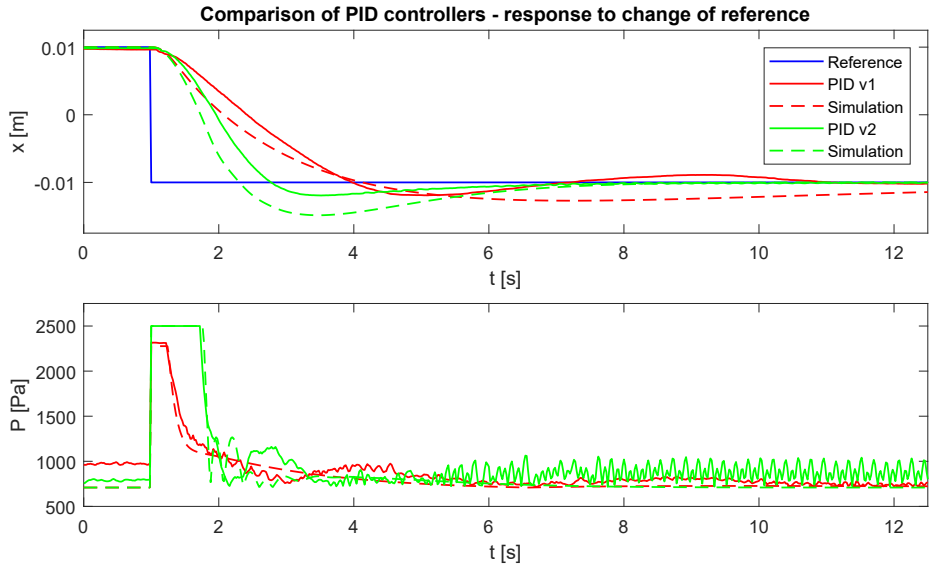

Figure 7.1: Comparison between the two PID controllers.

propagation delay is not precisely compensated. The control action of *PID v2* is greater and saturated for longer than the control action of *PID v1*.

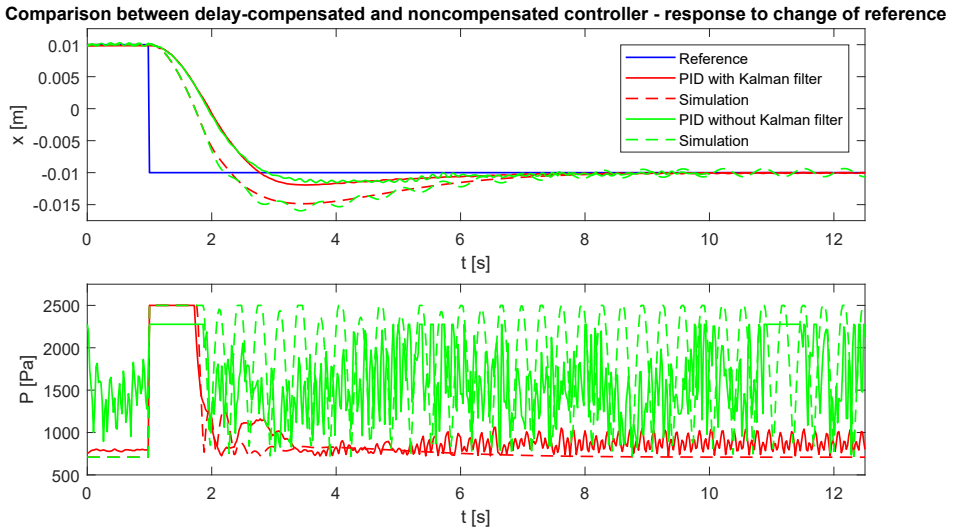

Figure 7.2: Comparison between controllers with and without propagation delay compensation.

Next, the influence of the delay compensation was investigated. The same experiment as before was conducted on controllers with and without delay compensation. Their responses are illustrated in Figure 7.2. Only the responses of *PID v2* are shown, as the difference in behaviour was more apparent in this case. On the real system, we can see smaller overshoot and slower rise time, which we already discussed. Both the real and the simulated systems without compensation oscillate, but the real system has a smaller

amplitude than the simulation. This could, once again, indicate that the actual propagation delay is smaller than the model predicts. The control action of the non-compensated controller is much greater and changes faster than the control action of the compensated controller. While the control action in the simulation of the non-compensated controller has a sinusoidal characteristic, the control action of the real system resembles white noise, which could be caused by errors in the position measurement.

7.2 Following a trajectory

In this experiment, the ability of the controller to track a moving reference was tested. The reference moves along a trajectory shaped like the infinity symbol, ∞. The experiment was conducted with the reference moving at $5\,\mathrm{mm\,s^{-1}}$, and $10\,\mathrm{mm\,s^{-1}}$ on controllers utilizing delay compensation.

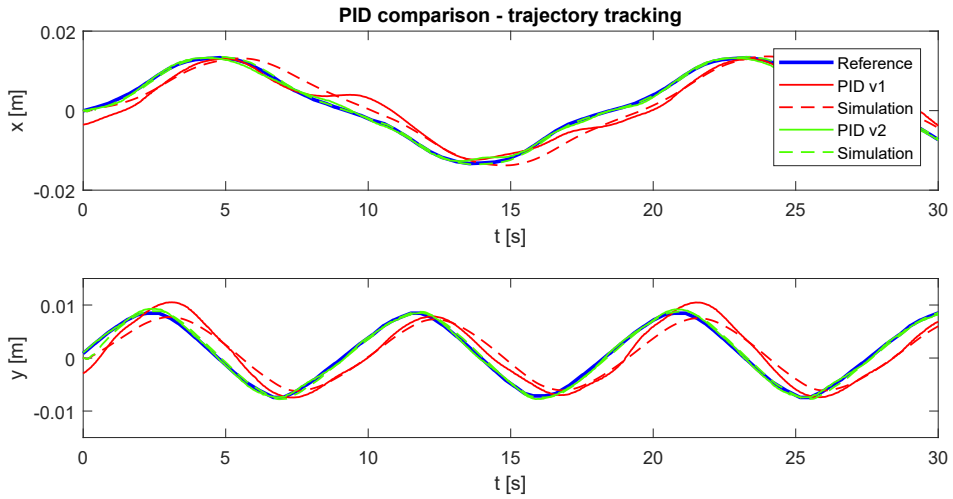

Figure 7.3: The x- and y-coordinates of the manipulated object following a reference, which moves at $5\,\mathrm{mm\,s^{-1}}$.

In Figure 7.3, we can see the results of the experiment with the reference moving at $5\,\mathrm{mm\,s^{-1}}$. *PID v2* follows the reference with minimum error both in the simulation and on the real system. In the simulation, *PID v1* follows the trajectory with a constant lag. On the real system, the controller sometimes follows the reference in one coordinate, while it is off in the other coordinate.

When the reference speeds up to $10\,\mathrm{mm\,s^{-1}}$, the issues become more significant. The lag of *PID v1* is higher than in the previous case. *PID v2* follows the reference with greater error as well and overshoots at the end of

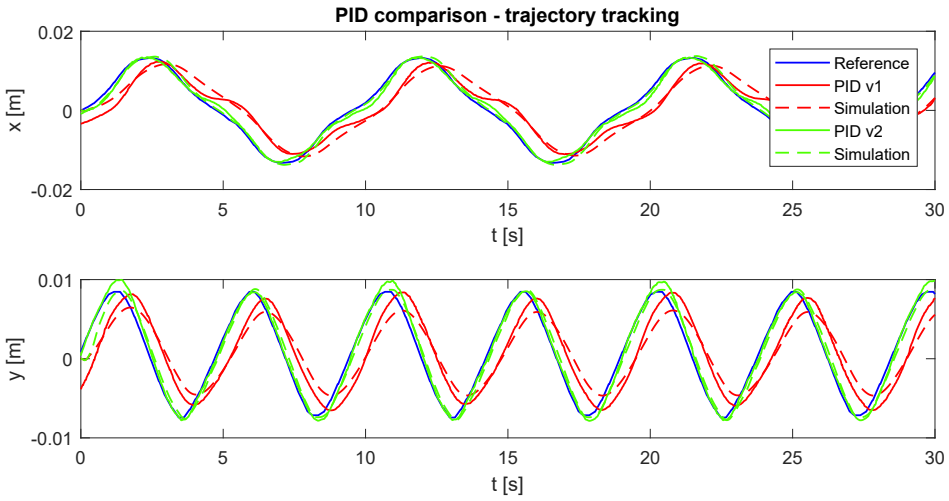

Figure 7.4: The x- and y-coordinates of the manipulated object following a reference, which moves at $10\,\mathrm{mm\,s^{-1}}$.

the loop in y-coordinate. The results are shown in Figure 7.4.

7.3 The positioning capabilities

The height of the transducer array is set to 65 mm which, as we discussed in Chapter 2, affects the active manipulation area. In this series of experiments, we determine the manipulation area and measure how precisely can the controller position the particle. Utilizing the symmetry, the measurements were done in the first quadrant of the manipulation area only using the *PID v1* with delay compensation.

To determine the manipulation area, we gradually increase the distance of the reference point from the coordinate origin along the x-axis, y-axis and the diagonal, until the controller cannot stabilize the particle. In all three experiments, the maximum distance was 21 mm. This leads to an assumption that the effective manipulation area is a circle with a radius of 21 mm. To test the assumption, we set the reference points along the circle. Unlike the experiment with trajectory following, where the reference moved regardless of the particle's position, the reference point in this experiment does not move until the particle is close to it. The footage of the experiment is in the materials on the supplementary CD. Although the controller needed longer time to stabilize the particle, it was able to complete the circle.

To test the precision of the controller, we created a 15-by-15 mm rectangular grid of reference points distant 1 mm from each other. Then, we let the controller stabilize the particle at each reference point for 10 seconds and we calculated the mean distance from the reference.

The results are shown in Figure 7.5. The green crosses represent the individual reference points, the radii of the red circles represent the mean distance of the particle from the reference. As we can see, there is no clear pattern or dependence of the mean error on the distance from the centre. The values of the mean error are between 0.1 mm and 0.5 mm.

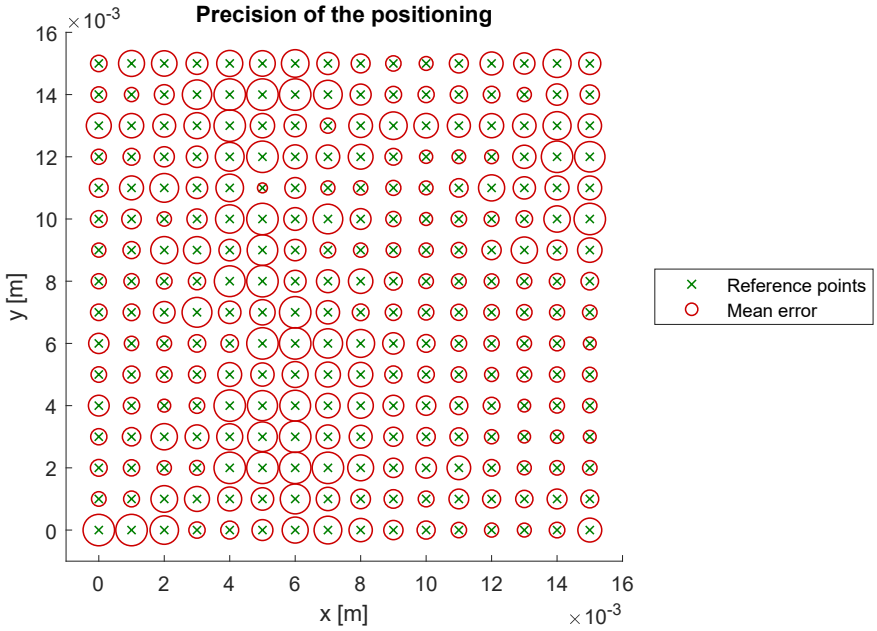

Figure 7.5: Results of the positioning precision experiment.

Chapter 8

Conclusion

In this thesis, I thoroughly described the process of creating the platform and performing experiments. I designed and built most of the mechanical components, programmed the optimization algorithm, and modified the communication script. I created a simulation model of a floating particle and identified its parameters. Then, I designed a controller based on the model and tested its ability to manipulate with a floating object. The controller was able to stabilize the object at any point within the 20 mm distance from the centre with maximum error of 0.5 mm. The controller was also able to track a reference moving at a speed of up to $10\,\mathrm{mm\,s^{-1}}$.

There are still many improvements that could have been done, and ideas that could have been tried. For instance, I could have designed more controllers using different methods. However, as a simple PID controller functions well, I did not feel the need to try other control algorithms. Due to the tight schedule, I was unable to test the positioning of two or more floating objects.

In its current state, the experimental platform does not have any obvious industrial or scientific application. However, it should be pointed out that the entire platform was built from commercially available parts, while the experiments in most of the cited articles are conducted on custom-made, more precise hardware. Furthermore, the model of the acoustic field is simplified, compared to other research. This project serves as a proof of concept that applying the control theory to ultrasonic manipulation is possible.

Appendix A

Bibliography

[1] Asier Marzo et al. “Holographic acoustic elements for manipulation of levitated objects”. In: *Nature Communications* 6 (Oct. 27, 2015), p. 8661. ISSN: 2041-1723. DOI: 10.1038/ncomms9661.

[2] Asier Marzo et al. “Ghost Touch: Turning Surfaces into Interactive Tangible Canvases with Focused Ultrasound”. In: *Proceedings of the 2015 International Conference on Interactive Tabletops & Surfaces*. ITS ’15. New York, NY, USA: ACM, 2015, pp. 137–140. ISBN: 978-1-4503-3899-8. DOI: 10.1145/2817721.2817727.

[3] Jiří Zemánek, Tomáš Michálek, and Zdeněk Hurák. “Feedback control for noise-aided parallel micromanipulation of several particles using dielectrophoresis”. In: *Electrophoresis* 36 (July 2015), pp. 1451–1458. DOI: 10.1002/elps.201400521.

[4] Jiří Zemánek, Sergej Čelikovský, and Zdeněk Hurák. “Time-optimal Control for Bilinear Nonnegative-in-control Systems: Application to Magnetic Manipulation”. In: *20th IFAC World Congress*. Vol. 50. Toulouse, France, July 2017, pp. 16032–16039. DOI: 10.1016/j.ifacol.2017.08.1916.

[5] August Kundt. “Ueber eine neue Art akustischer Staubfiguren und über die Anwendung derselben zur Bestimmung der Schallgeschwindigkeit in festen Körpern und Gasen”. In: *Annalen der Physik* 203.4 (1866), pp. 497–523. ISSN: 1521-3889. DOI: 10.1002/andp.18662030402.

[6] Marco A. B. Andrade, Nicolás Pérez, and Julio C. Adamowski. “Review of Progress in Acoustic Levitation”. In: *Brazilian Journal of Physics* (Dec. 30, 2017), pp. 1–24. ISSN: 0103-9733, 1678-4448. DOI: 10.1007/s13538-017-0552-6.

[7] T. Wang, M. Saffren, and D. Elleman. "Acoustic chamber for weightless positioning". In: *12th Aerospace Sciences Meeting*. American Institute of Aeronautics and Astronautics, 1974. DOI: 10.2514/6.1974-155.

[8] Takayasu Matsui et al. "Translation of an Object Using Phase-Controlled Sound Sources in Acoustic Levitation". In: *Japanese Journal of Applied Physics* 34.5 (May 1995), p. 2771. ISSN: 1347-4065. DOI: 10.1143/JJAP.34.2771.

[9] Charles R. P. Courtney et al. "Independent trapping and manipulation of microparticles using dexterous acoustic tweezers". In: *Applied Physics Letters* 104.15 (Apr. 14, 2014), p. 154103. ISSN: 0003-6951. DOI: 10.1063/1.4870489.

[10] Yoshiki Hashimoto, Yoshikazu Koike, and Sadayuki Ueha. "Acoustic levitation of planar objects using a longitudinal vibration mode". In: *Journal of the Acoustical Society of Japan (E)* 16.3 (1995), pp. 189–192. ISSN: 0388-2861, 2185-3509. DOI: 10.1250/ast.16.189.

[11] Takafumi Amano et al. "A Multi-Transducer Near Field Acoustic Levitation System for Noncontact Transportation of Large-Sized Planar Objects". In: *Japanese Journal of Applied Physics* 39.5 (May 2000), p. 2982. ISSN: 1347-4065. DOI: 10.1143/JJAP.39.2982.

[12] Masaya Takasaki et al. "Non-contact ultrasonic support of minute objects". In: *Physics Procedia*. International Congress on Ultrasonics, Santiago de Chile 3.1 (Jan. 2009), pp. 1059–1065. ISSN: 1875-3892. DOI: 10.1016/j.phpro.2010.01.137.

[13] Shinichiro Chino et al. "Actuation force characteristics of ultrasonic suspension for minute object". In: *2011 IEEE International Ultrasonics Symposium*. 2011 IEEE International Ultrasonics Symposium. Oct. 2011, pp. 1218–1221. DOI: 10.1109/ULTSYM.2011.0300.

[14] Marco A. B. Andrade, Anne L. Bernassau, and Julio C. Adamowski. "Acoustic levitation of a large solid sphere". In: *Applied Physics Letters* 109 (July 1, 2016), p. 044101. ISSN: 0003-6951. DOI: 10.1063/1.4959862.

[15] Asier Marzo et al. "Realization of compact tractor beams using acoustic delay-lines". In: *Applied Physics Letters* 110.1 (Jan. 2, 2017), p. 014102. ISSN: 0003-6951. DOI: 10.1063/1.4972407.

[16] Benjamin Long et al. "Rendering Volumetric Haptic Shapes in Mid-air Using Ultrasound". In: *ACM Trans. Graph.* 33.6 (Nov. 2014), 181:1–181:10. ISSN: 0730-0301. DOI: 10.1145/2661229.2661257.

[17] Charles R. P. Courtney et al. "Dexterous manipulation of microparticles using Bessel-function acoustic pressure fields". In: *Applied Physics Letters* 102.12 (Mar. 25, 2013), p. 123508. ISSN: 0003-6951. DOI: 10.1063/1.4798584.

[18] Adam Kollarčík. "Planární akustická manipulace s kulovými objekty na pevném povrchu". Bachelor's Thesis. Czech Technical University in Prague, 2018.

[19] *Murata MA40S4S product specifications*. URL: https://www.murata.com/products/productdetail?partno=MA40S4S (visited on 04/24/2018).

[20] Jakub Drs. "64-kanálový generátor - VHDL project". Available on the Supplementary CD. Mar. 2012.

[21] Jakub Drs. "64-kanálový generátor". Available on the Supplementary CD. Jan. 2012.

[22] Lawrence E. Kinsler et al. *Fundamentals of acoustics*. 4th Edition. Wiley, 2000. 568 pp. ISBN: 0-471-84789-5.

[23] P. Singh and D. D. Joseph. "Fluid dynamics of floating particles". In: *Journal of Fluid Mechanics* 530 (May 2005), pp. 31–80. ISSN: 1469-7645, 0022-1120. DOI: 10.1017/S0022112005003575.

[24] Chin Hong Ooi et al. "Measuring the Coefficient of Friction of a Small Floating Liquid Marble". In: *Scientific Reports* 6 (Dec. 2, 2016), p. 38346. ISSN: 2045-2322. DOI: 10.1038/srep38346.

[25] Jordan T. Petkov et al. "Measurement of the Drag Coefficient of Spherical Particles Attached to Fluid Interfaces". In: *Journal of Colloid and Interface Science* 172.1 (June 1, 1995), pp. 147–154. ISSN: 0021-9797. DOI: 10.1006/jcis.1995.1237.

[26] Louis V. King, S. F. R. "On the acoustic radiation pressure on spheres". In: *Proceedings of the Royal Society London A* 147.861 (Nov. 15, 1934), pp. 212–240. ISSN: 0080-4630, 2053-9169. DOI: 10.1098/rspa.1934.0215.

[27] Henrik Bruus. "Acoustofluidics 7: The acoustic radiation force on small particles". In: *Lab on a Chip* 12.6 (Feb. 21, 2012), pp. 1014–1021. ISSN: 1473-0189. DOI: 10.1039/C2LC21068A.

Appendix B

Nomenclature

Abbreviations

AA4CC	Advanced Algorithms for Control and Communication research group, `http://aa4cc.dce.fel.cvut.cz`
3D	three-dimensional
2D	two-dimensional
LED	light-emitting diode
CD	compact disc
CMOS	complementary metal-oxide-semiconductor
USB	Universal Serial Bus
RS-232	Recommended Standard 232
UART	universal asynchronous receiver-transmitter
BFGS	Broyden–Fletcher–Goldfarb–Shanno optimization algorithm
L-BFGS	limited memory BFGS
PID	proportional–integral–derivative controller

Symbols

Symbol	Description	Unit
$\mathbb{N}$	natural numbers	—
$\mathbb{R}$	real numbers	—
j	imaginary unit	—

Symbol	Description	Unit
$\tilde{p}$	phasor of the overall acoustic pressure	Pa
p	overall acoustic pressure	Pa
i	index of the transducer; $i \in \mathbb{N}$	—
N	number of transducers; $N \in \mathbb{N}$	—
$\tilde{p}_i$	phasor of the complex acoustic pressure contribution form the i^{th} transducer	Pa
$\mathfrak{Re}\{.\}$	real part	—
$\mathfrak{Im}\{.\}$	imaginary part	—
φ_i	phase delay of the i^{th} transducer	rad
ϕ	vector of the phase delays; $\phi \in \mathbb{R}^N$	rad
ω	angular frequency of the emitted soundwave	$\mathrm{rad\,s^{-1}}$
t	time	s
M_i	complex pressure of the i^{th} transducer equivalent to no phase delay	Pa
A	transducers' power	$\mathrm{Pa\,m}$
f_{dir}	transducers' directivity function	—
θ_i	angular deviation from the i^{th} transducer's axis	rad
d_i	distance from the i^{th} transducer	m
k	wavenumber of the emitted soundwave	$\mathrm{m^{-1}}$
x_a, y_a, z_a	coordinates; $a \in \{t, p, \varnothing\}$	m
ρ_0	air density	$\mathrm{kg\,m^{-3}}$
c	speed of sound in air	$\mathrm{m\,s^{-1}}$
U_0	velocity amplitude of the transducer's vibrating plate	$\mathrm{m\,s^{-1}}$
r	radius of the transducer's vibrating plate	m
J_1	first order Bessel function of the first kind	—
L	number of points with the required pressure; $M \in \mathbb{N}$	—
k	index of the point with the required pressure; $k \in \mathbb{N}$	—
P_k	required acoustic pressure at the k^{th} point	Pa
$\mathcal{O}$	optimization algorithm criterion function	$\mathrm{Pa^2}$
$\mathbf{F}_{\mathrm{D}}$	Stokes' drag force	N
$F_{\mathrm{D}a}$	components of the Stokes' drag; $a \in \{x, y\}$	N
$\mathbf{F}$	force caused by the acoustic pressure field	N
F_a	components of the pressure field force; $a \in \{x, y\}$	N
m	mass of the floating object	kg
R	radius of the floating object	m
μ	dynamic viscosity	$\mathrm{Pa\,s}$
β	drag force correction constant	—
b	coefficient of drag	$\mathrm{N\,s\,m^{-1}}$
s	complex frequency	$\mathrm{s^{-1}}$
U	acoustic pressure potential	$\mathrm{N\,m}$
K_1	acoustic pressure potential constant	$\mathrm{m^4 s^2/kg}$
V	acoustic velocity potential	$\mathrm{N\,m}$
K_2	acoustic velocity potential constant	kg
$\mathbf{v}$	acoustic velocity	$\mathrm{m\,s^{-1}}$

Symbol	Description	Unit
P_{lin}	radiation force to pressure relation linear coefficient	m^{-2}
P_{off}	radiation force to pressure relation constant offset	Pa
$\widehat{H}$	estimated model transfer function	$\text{m}\,\text{Pa}^{-1}$
$\widehat{a}$	numerator of the estimated transfer function	$\text{m}^2\,\text{kg}^{-1}$
$\widehat{b}$	estimated transfer function denominator's linear coefficient	s^{-1}
$\widehat{c}$	estimated transfer function denominator's constant coefficient	s^{-2}
$\mathbf{x}$	states of the discretized model	—
$\mathbf{A}$	state matrix of the discretized model	—
$\mathbf{B}$	input matrix of the discretized model	—
$\mathbf{C}$	output matrix of the discretized model	—
u	input of the discretized model	—
y	output of the discretized model	—
n	discrete-time step; $n \in \mathbb{N}_0$	—
$\bar{\mathbf{A}}$	state matrix of the extended discretized model	—
$\bar{\mathbf{B}}$	input matrix of the extended discretized model	—
$\mathbf{C}_{\text{del}}$	delayed output matrix of the extended discretized model	—
$\mathbf{C}_{\text{und}}$	undelayed output matrix of the extended discretized model	—
K_{P}	proportional constant of the PID controller	$\text{N}\,\text{m}^{-1}$
K_{I}	integral constant of the PID controller	$\text{N}\,\text{m}^{-1}\,\text{s}^{-1}$
K_{D}	derivative constant of the PID controller	$\text{N}\,\text{s}\,\text{m}^{-1}$
F_{sat}	controller's output force saturation	N

Appendix C

Contents of the supplementary CD

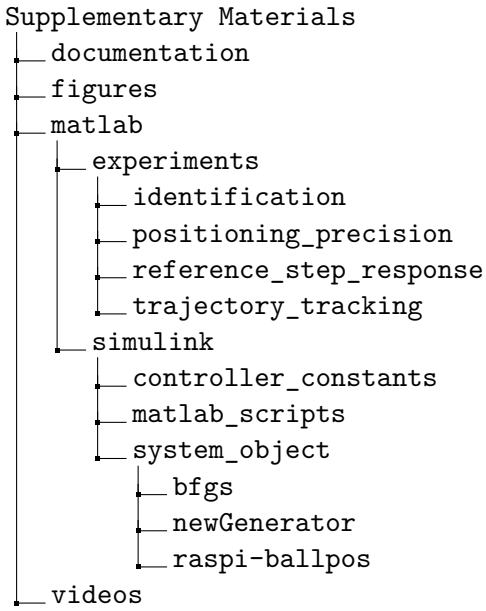

Figure C.1: The directory tree of the supplementary CD.

Figure C.1 shows the overall structure of the supplementary CD. The root folder contains this thesis in PDF format. The `documentation` directory contains two manuals to the 64-channel generator originally used in the dielectrophoresis project [20, 21] in PDF format. The `figures` directory contains all images used in this thesis in their original format (SVG for vector graphics, JPEG for photographs, PNG for bitmaps, and FIG for MATLAB figures). The `matlab` folder contains all files associated with MATLAB. The `experiments` subfolder contains the data from conducted experiments and MATLAB scripts for plotting the results. The `simulink` subfolder contains all

necessary files for deploying the control scheme to the Raspberry Pi computer, including the Simulink models, constants of the controller, the MATLAB script for transforming the coordinates, and the System Objects for solving the optimization problem, communicating with the 64-channel generator and measuring the position of the manipulated object. The `videos` folder contains the footage of the experiments.

BACHELOR'S THESIS ASSIGNMENT

I. Personal and study details

Student's name: **Matouš Josef** Personal ID number: **457195**

Faculty / Institute: **Faculty of Electrical Engineering**

Department / Institute: **Department of Control Engineering**

Study program: **Cybernetics and Robotics**

Branch of study: **Systems and Control**

II. Bachelor's thesis details

Bachelor's thesis title in English:

Manipulation with objects on a surface of a liquid using an array of ultrasonic transducers

Bachelor's thesis title in Czech:

Manipulace s objekty na hladině kapaliny pomocí pole ultrazvukových aktuátorů

Guidelines:

Design and build an experimental platform enabling feedback control of a movement of small objects on a surface of a liquid using an acoustic pressure controlled by an array of ultrasonic transducers.
1. Finish the design and construction of the hardware of the experimental platform (i.e. a placement of the array of transducers and a camera considering the container with objects of interest).
2. Explore and document the abilities of the platform exploitable for non-contact manipulation with floating objects.
3. Create a control-oriented simulation model incorporating all the predominant physical phenomena identified as useful for manipulation in the previous task.
4. Design and implement a control algorithm for steering and positioning the objects using visual feedback from the camera.
5. Perform experiments with control of one or more objects and evaluate the results.

Bibliography / sources:

[1] Marzo, Asier, Richard McGeehan, Jess McIntosh, Sue Ann Seah, and Sriram Subramanian. "Ghost Touch: Turning Surfaces into Interactive Tangible Canvases with Focused Ultrasound." In Proceedings of the 2015 International Conference on Interactive Tabletops & Surfaces, 137-140. ITS '15. New York, NY, USA: ACM, 2015. https://doi.org/10.1145/2817721.2817727.
[2] Marzo, Asier, Sue Ann Seah, Bruce W. Drinkwater, Deepak Ranjan Sahoo, Benjamin Long, and Sriram Subramanian. "Holographic Acoustic Elements for Manipulation of Levitated Objects." Nature Communications 6 (October 27, 2015): 8661. https://doi.org/10.1038/ncomms9661.
[3] Marshall, Mark, Thomas Carter, Jason Alexander, and Sriram Subramanian. "Ultra-Tangibles: Creating Movable Tangible Objects on Interactive Tables." In Proceedings of the SIGCHI Conference on Human Factors in Computing Systems, 2185-2188. CHI '12. New York, NY, USA: ACM, 2012. https://doi.org/10.1145/2207676.2208370.
[4] Long, Benjamin, Sue Ann Seah, Tom Carter, and Sriram Subramanian. "Rendering Volumetric Haptic Shapes in Mid-Air Using Ultrasound." ACM Trans. Graph. 33, no. 6 (November 2014): 181:1-181:10. https://doi.org/10.1145/2661229.2661257.

Name and workplace of bachelor's thesis supervisor:

Ing. Tomáš Michálek, Department of Control Engineering, FEE

Name and workplace of second bachelor's thesis supervisor or consultant:

Date of bachelor's thesis assignment: **16.01.2018** Deadline for bachelor thesis submission: **25.05.2018**

Assignment valid until: **30.09.2019**

Ing. Tomáš Michálek	prof. Ing. Michael Šebek, DrSc.	prof. Ing. Pavel Ripka, CSc.
Supervisor's signature	Head of department's signature	Dean's signature

III. Assignment receipt

The student acknowledges that the bachelor's thesis is an individual work. The student must produce his thesis without the assistance of others, with the exception of provided consultations. Within the bachelor's thesis, the author must state the names of consultants and include a list of references.

. _____
Date of assignment receipt

_____
Student's signature

